Spring 6-12-2018

Dark Current RTS-Noise in Silicon Image Sensors

Benjamin William Hendrickson
Portland State University

Dark Current RTS-Noise in Silicon Image Sensors

by

Benjamin William Hendrickson

A thesis submitted in partial fulfillment of the
requirement for the degree of

Master of Science
in
Physics

Thesis Committee:
Erik Bodegom, Chair
Ralf Widenhorn
Morley M. Blouke

Portland State University
2018

ABSTRACT

Random Telegraph Signal (RTS) noise is a random noise source defined by discrete and metastable changes in the magnitude a signal. Though observed in a variety of physical processes, RTS is of particular interest to image sensor fabrication where progress in the suppression of other noise sources has elevated its noise contribution to the point of approaching the limiting noise source in scientific applications [3].

There have been two basic physical sources of RTS noise reported in image sensors. The first involves a charge trap in the oxide layer of the source follower in a CMOS image sensor. The capture and emission of a charge changes the conductivity across the source follower, altering the signal level. The second RTS source in image sensors has been reported in CCD and CMOS architectures and involves some metastability in the structure of the device within the light collection area.

A methodology is presented for the analysis of RTS noise. Utilizing wavelets, a time-based signal has white noise removed, while RTS transitions are preserved. This allows for the simple extraction of RTS parameters, which provide valuable insight into defects in semiconductor devices. The scheme is used to extract RTS transition amplitudes and time constants from radiation damaged CMOS image sensor pixels.

Finally, the generation of ionizing radiation induced RTS centers is investigated and discussed. Surprisingly, the number of RTS centers does not scale linearly with absorbed dose, but instead follows a quadratic dependence. The implications and possible mechanisms behind the generation of these RTS centers are discussed.

DEDICATION

For Kirsten. I would have never started down this road without you, and would have no reason to finish. This is for you alone.

ACKNOWLEDGMENTS

I would like to thank Dr. Bodegom for his encouragement, guidance and uncanny humor these past years, all of which have been essential components in educating and driving me to the completion of this work.

I would like to thank Dr. Widenhorn for his wisdom and unyielding scientific skepticism which have driven me to constantly strive toward an unassailable burden of proof in all of my experimental endeavors.

I would like to thank Dr. Morley Blouke for his incredible patience as an educator, his unearned faith as a mentor, and for serving as an invaluable living example of what it means to achieve true excellence as a scientific professional.

I would like to thank Dr. Richard Crilly of OHSU for his assistance with irradiating my sensors without which this work would not be possible.

I would like to thank Leroy Laush, Alex Chally, Dr. Nicholas Day, and Joshua Olsen for their intellectually stimulating friendship, guidance, and technical assistance. Also, Paul DeStefano, Denis Heidtmann, Joe Niederriter, Dr. Justin Dunlap, Dr. Elliot Mylott, and Dr. Bahareh Ajdari for creating a warm and collaborative lab environment in which a new and naïve graduate student could make a second home.

Additionally, I would like to thank my parents Gayland and Linda Hendrickson and sister Betsy for a lifetime of loving support and guidance, and encouraging my restless and constant intellectual struggle.

TABLE OF CONTENTS

LIST OF FIGURES

CHAPTER ONE – INTRODUCTION

1.1 Light and Semiconductors

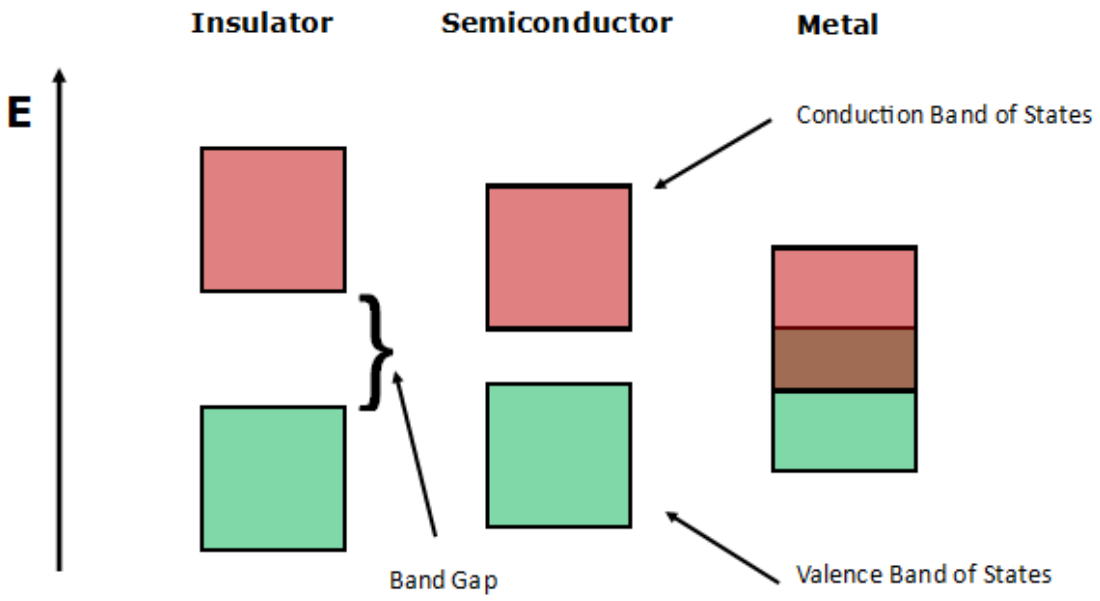

Figure 1: The three basic kinds of solids, denoted by their electronic state configurations

All image sensors rely on the same physical process, the conversion of light to electrical charge via the internal photoelectric effect. This process, similar to its namesake, is defined by the absorption of energy from a photon by an atom, in order to excite an electron from a bound state in the valence band, to a semi-free state in the conduction band. Photons in the optical range of the electromagnetic spectrum have energies between $1.7eV$ (electron volts) and $3.2eV$.

The minimum amount of energy required to promote a charge is a quantity known as the band-gap. All materials are electronically classified by their band-gap. Insulators are so called because their band gap is large, which means excitation is a highly unlikely event and very few electrons are likely to be available for conduction. Conductors conversely have very small band gaps, or even overlapping band gaps, meaning that, in room temperature conditions, electrons are free to move around the material. Semiconductors are a special class of material because they occupy a 'Goldilocks' region between insulator and conductor where electron promotion can be tuned and controlled via doping to create electronic devices. There is a very large selection of semiconductors that exhibit an equally large variety of properties which may or may not be useful for an application. This manuscript focuses exclusively on silicon which, with its band gap of $1.1eV$, is well suited for the development of solid state image sensors in the spectral range of $1\mu m$ in the near infrared to $\sim 10nm$ in the soft x-ray regime.

1.2 Solid State Image Sensors

There are two common varieties of solid state image sensors, charge coupled devices (CCDs) and complementary metal oxide semiconductor (CMOS) imagers. Both kinds of sensors perform the same basic function: collect light inside a rectangular grid of picture elements (pixels) in order to construct an image in a paint-by-numbers fashion. What differs between the two designs is the circuitry involved in the collecting and counting of light particles. What follows is a brief overview of the two primary device

structures, and the various benefits and drawbacks that come from a particular design decision.

1.2.1 CMOS Image Sensor Architecture & Operation Basics

All CMOS image sensors share a few of the same basic elements: an array of pixels, row and column addressing circuitry, and an analog-to-digital converter (ADC). Each pixel in CMOS architecture contains: a photodiode, a reverse biased PN-diode where photons are converted to electron-hole pairs, an amplifier, a reset switch, and a row select transistor. While pixel architecture has evolved over the last couple decades [1], all CMOS sensors contain the basic elements seen in this most basic design, called the 3T (for transistor) pixel structure.

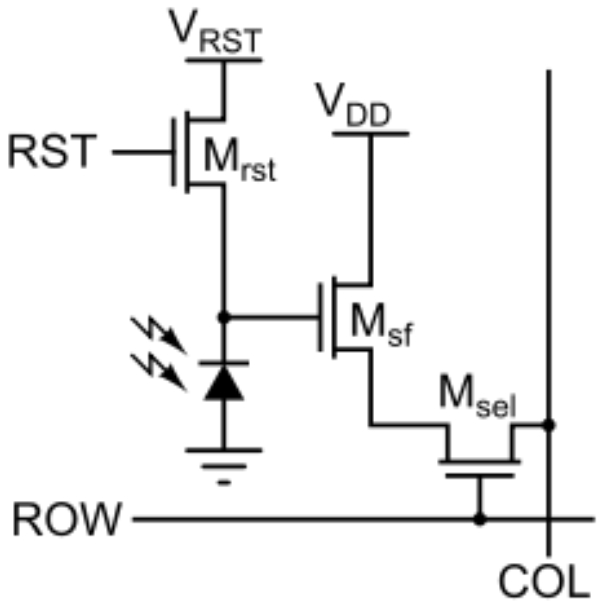

Figure 2: The equivalent circuit for a 3T CMOS pixel structure

Operation of a 3T APS sensor employs a so-called rolling shutter clocking method that executes as follows:

1: A voltage pulse is applied to the gate of the reset transistor ensuring that a reverse biasing voltage V_{RST} is placed across the photodiode.

2: The pixel is exposed to incident light for a given integration time t_{int}. During t_{int}, energy from discrete photons is absorbed by an atom to promote an electron to the conduction band, effectively depositing a hole in its place. Both the electron and the hole are essentially free to move, the electron in the conduction band, the hole in the valence band. In a typical configuration, electrons are collected while holes are discarded to ground.

3: The charge built up during t_{int} changes the voltage on the gate of the source follower (SF) transistor. The SF translates the charge from tens to hundreds of electrons to a more manageable voltage to be measured by the ADC.

4: The voltage is now at the row select transistor. All row select transistors are turned on simultaneously for a particular row. The column bus then reads out their voltages by sequentially sampling each one. This voltage is converted to a digital number by the on-chip ADC, which is interpreted to represent light intensity by a computer.

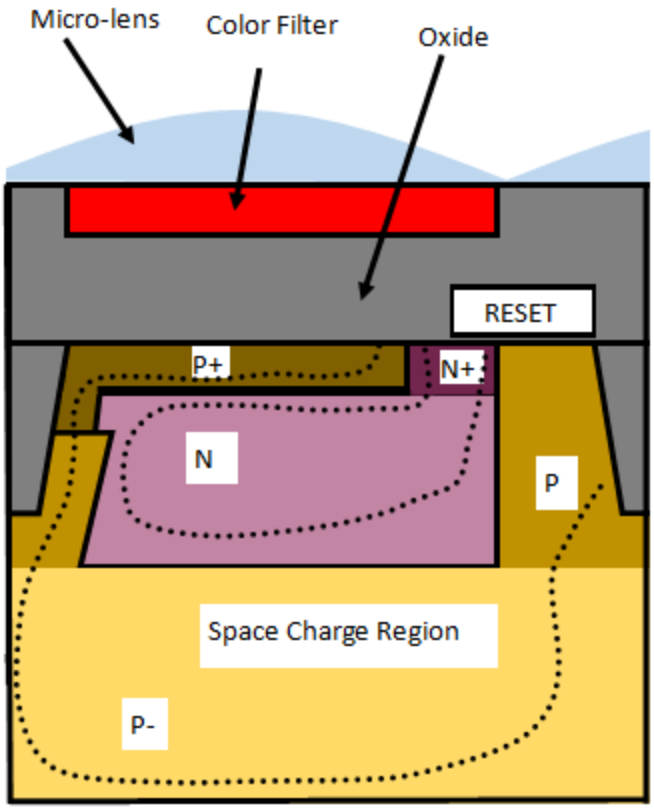

Figure 3: Cross section of a frontside illuminated 3T CMOS pixel

CMOS image sensors are fabricated with the widely used CMOS process, which can significantly lower the cost of production. This, along with the low power consumption during operation makes them ideal for consumer applications such as DSLR cameras and phone cameras. They are, however, also subject to unique noise sources, arising from fabrication inconsistencies, which require specific consideration. Reset noise, which stems from the integration of white noise is unique to CMOS sensors [2]. Additionally, there is no process that can make an identical source follower amplifier for millions of pixels, meaning that each pixel has a unique gain.

1.2.2 CCD Image Sensor Architecture & Operation Basics

Charge Coupled Devices (CCDs) convert photons into charge in the same way that CMOS imagers do. A PN-diode is held in reverse bias, creating a wide space charge region (SCR). As shown below

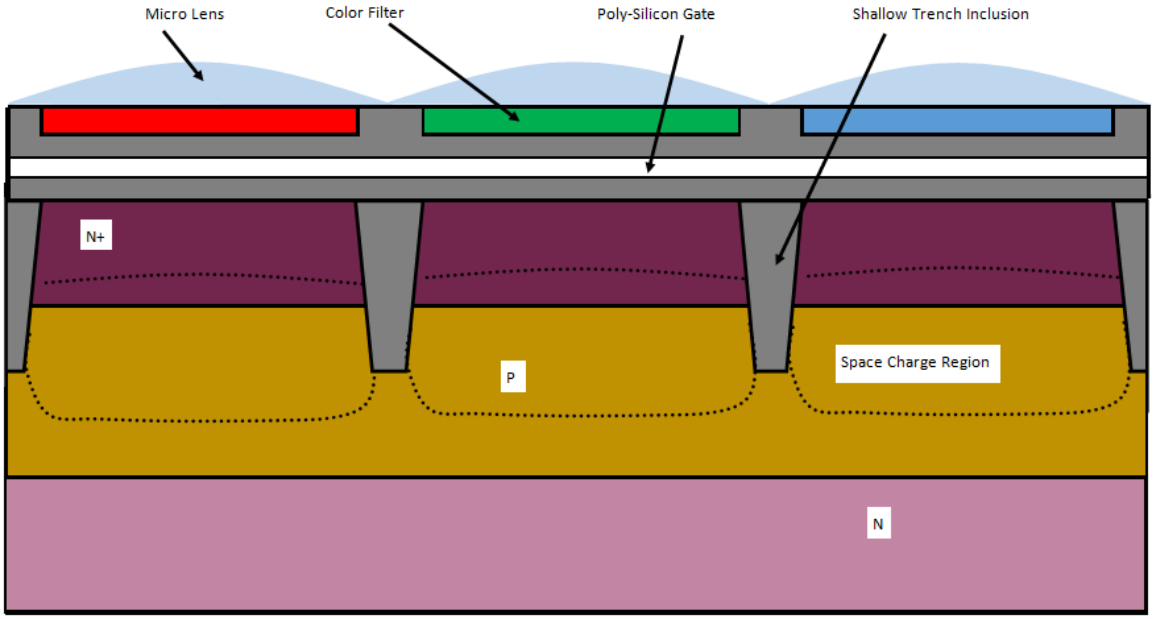

Figure 4: Cross section of a CCD architecture

Charge Coupled Devices (CCDs) perform the same basic functions as CMOS image sensors, but differ starkly in how the charge, or incident photon count, stored in a pixel is read out to a computer system. Rather than go immediately to an amplification stage after integration, promoted electrons from any one pixel are carefully shuttled through the device and amplified just before the end of the read-out stage. To move the charge from the pixel to the computer, CCDs use a clocking sequence of voltages to move the charge pixel by pixel.

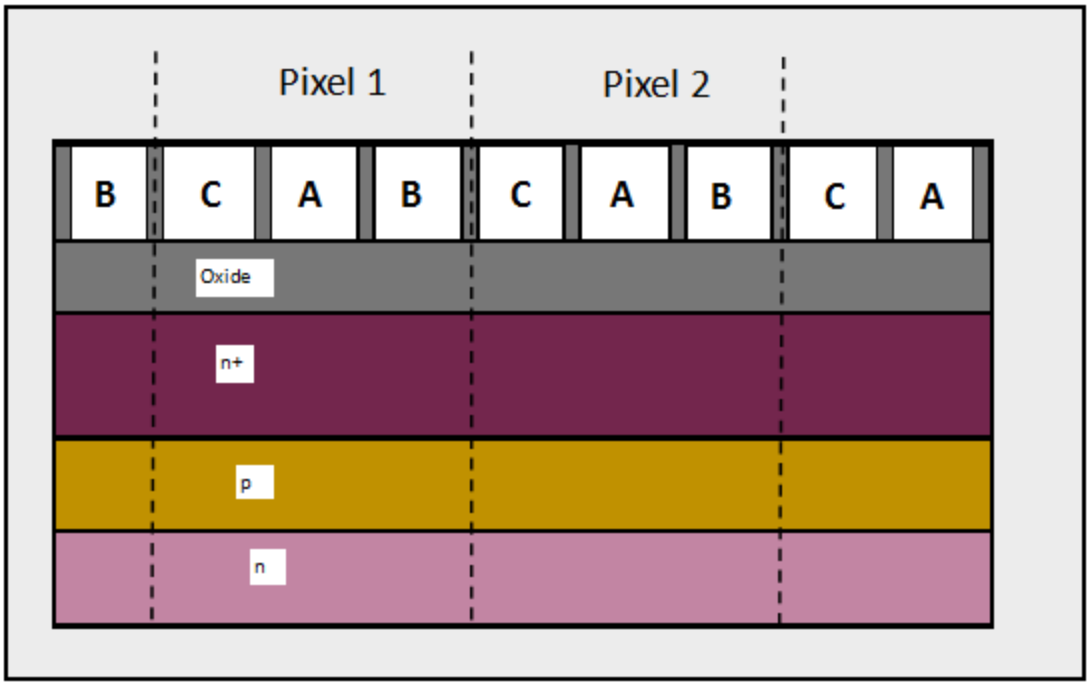

Figure 5: Charge transfer sequence

As seen in figure 5, there are multiple polysilicon traces above the oxide layer of the device. By connecting a voltage to these traces in a cyclical pattern ($\boldsymbol{A \rightarrow AB \rightarrow B \rightarrow BC \rightarrow C \rightarrow CA \rightarrow A}$ ...) the charge is moved along its column like a conveyer belt.

The entire imaging cycle unfolds as follows:

1: The device is exposed to light for t_{int} as described for CMOS sensors above.

2: The charge is moved, row-by-row, down it's column of the sensor until it reaches the bottom where the serial shift register is located. From here it's moved, one

column position at a time, until the charge reaches the amplifier, and the corresponding voltage is converted to a digital number by an external ADC which is read by a computer. It should be noted that this readout sequence also serves as the reset function for the sensor.

CCDs have some advantages and some drawbacks compared to CMOS sensors. They are generally lower noise devices, and enjoy the benefit of lacking the layers of metal traces required for CMOS operation which provides them a superior fill factor. Additionally, CCD pixels can be completely 'pinned' by putting a highly doped layer of semiconductor just beneath the oxide surface. Pinning ensures that the SCR does not come in contact with the oxide layer where defects are far more likely to lie. Because of pinning, the charge transfer process in CCDs is remarkable in its ability to not misplace charges.

Disadvantages of CCDs include cost, power consumption, and speed. Each CCD is a 'one-off' design, which means large up-front costs. Additionally, the original and the updated interline versions of CCD imagers can only be read out one row at a time, unlike CMOS sensors which are global shutter capable. This means that the CCD will always be slower than CMOS.

CHAPTER TWO – LEAKAGE CURRENT IN IMAGE SENSORS

2.1 Leakage Current Mechanisms

As discussed in chapter one, silicon is particularly suitable for image sensor fabrication because of its band gap. At $1.1eV$, the band gap is small enough to easily promote electrons to the conduction band given the absorption of any optical photon. $1.1eV$ is also large enough to ensure that promotion due to thermal excitation at room temperature is highly unlikely.

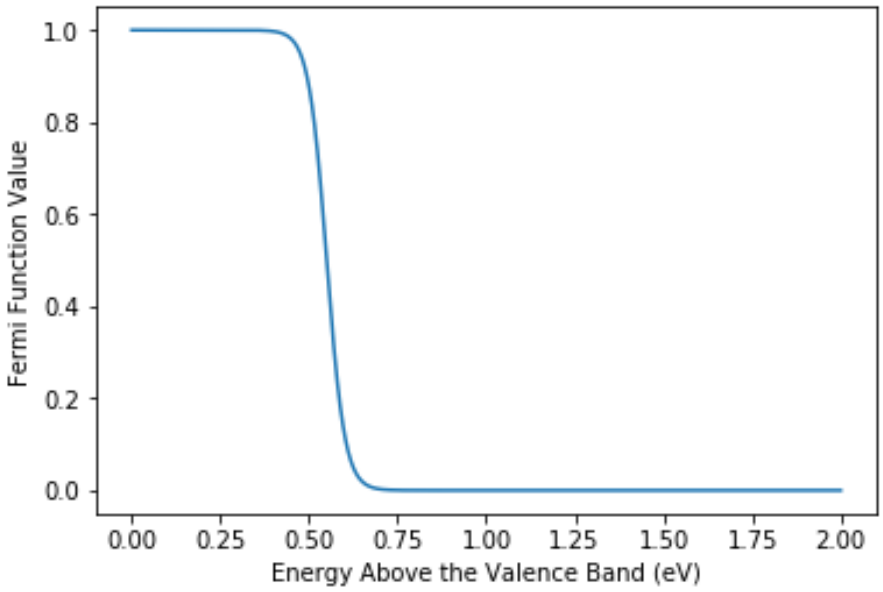

Figure 6: Fermi Function for silicon at 295K

Figure 6 is a plot of the Fermi function for silicon at 295K. The Fermi function describes the probability of the occupation of an energy state from thermal promotion. As the plot shows, the probability of an occupied state above the band gap is quite small and

tends to zero. In fact, integrating the occupation probabilities from $1.1eV - 2.0eV$ is a mere $1.0126 * 10^{-05}$.

It is important to note that the Fermi-Dirac statistics described above represent an ideal theoretical sandbox, and only hold if an important assumption is made, namely that the medium with which the electrons interact is structurally flawless. In practice this is far from the case, and there are a number of types of defects that influence device performance.

Within the energy band model, a defect is represented as a state within the forbidden region, providing an energetic 'stepping stone' to assist with promotion or conversely demotion of a conductive electron to the valence band. These trap states are an important limitation to device performance, since they allow electrons to be thermally promoted to the conduction band causing leakage current, or dark current.

The framework which describes these defect interactions is called Shockley-Read-Hall Generation/Recombination (SRH-G/R), and the rate of generation or recombination is dependent on several familiar variables: v_{th} is the thermal velocity, σ is the trap cross section, N_t is the trap density, n is the electron concentration, p is the hole concentration, n_i is the intrinsic carrier concentration, E_t is the trap energy level, E_i is the intrinsic Fermi level, k is Boltzmann's constant, and T is the temperature.

$$U = \frac{v_{th}\sigma N_t(np - n_i^2)}{n + p + 2n_i \cosh\left(\frac{E_t - E_i}{kT}\right)}$$

The rate of both generation and recombination is described by a single equation. If np is greater than n_i^2 there is net recombination. If np is less than n_i^2, there is net generation. Under normal operation, the light gathering areas in solid state image sensors are held in reverse bias, that is, within the SCR, $np \ll n_i^2$. The bias voltage is configured to widen the space charge region of the sensor as much as possible, which in turn increases the dynamic range of the device. An unavoidable consequence of a wide SCR is that the number of defects that lie inside it increases, and with them, an increase of leakage, or dark current. This is especially pronounced if the SCR comes in contact with an oxide interface where defects are far more common than in the bulk. When this happens the current generated on the interface will typically dwarf all other dark current sources. The current from this type of source is described as follows:

$$I_{it} = K_1 \exp\left(-\frac{E_g}{2kT}\right) A_{itdep} N_{it}$$

where K_1 is a process and design dependent constant, E_g is the band gap energy, A_{itdep} is the area of the interface inside the SCR, and N_{it} is the trap state density [3].

CHAPTER THREE – RANDOM TELEGRAPH SIGNAL NOISE

3.1 RTS Overview

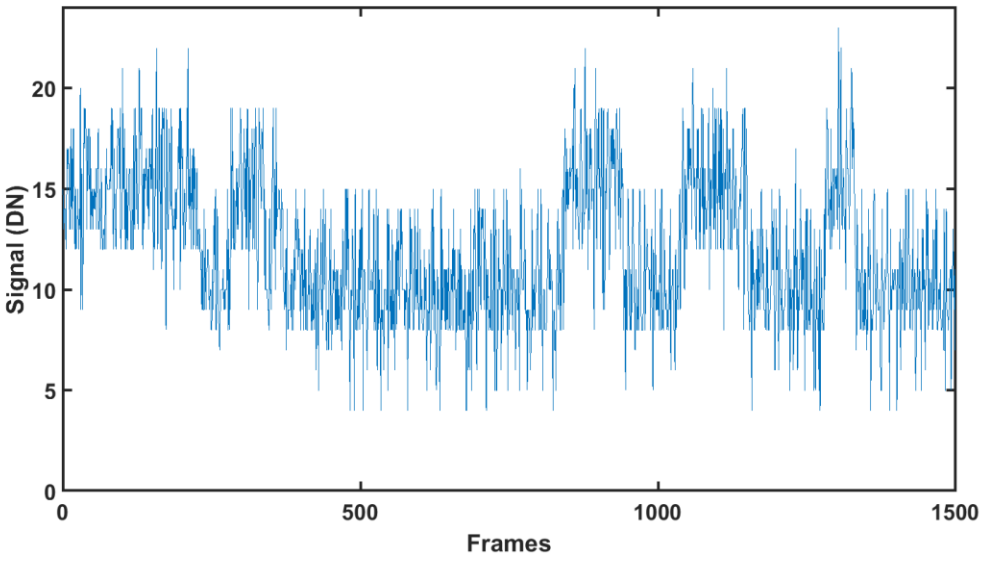

Figure 7: A prototypical bistable RTS-Noise Signal

Random Telegraph Signal (RTS) noise is characterized by discrete transitions in the signal current of a MOSFET device. First observed in point contact diodes, the steady shrinking of pixel pitch has driven RTS noise to become a major noise source in modern CMOS image sensors. These transitions occur due to alterations in the conductivity σ. Conductivity is expressed as $\sigma = \mu nq$ where μ is the mobility across the channel, n is the number of charge carriers, and q is the fundamental charge. RTS is known to have two primary causes, a change in μ brought on by the trapping/emission of a charge carrier in the gate oxide, and a change in n which arises from a metastable Shockley-Read-Hall (SRH) generation/recombination (G/R) center.

With regards to a CMOS image sensor, the change in mobility occurs in the source follower transistor, which acts as an amplifier for the charge induced by exposure to photons or dark current. As such, this flavor of RTS is called Source Follower RTS, or SF-RTS. If a charge becomes trapped in the gate oxide, the gate-source voltage V_{gs} is lowered, which decreases the mobility across the channel. Once the trapped charge is emitted, V_{gs} returns to its normal operating value and the signal again reads true, exempting of course other noise sources.

The physical mechanism behind the change in n is still inconclusive, but is likely to occur from the turning on and off of SRH G/R centers in the depleted region of a photodiode or on the Si/SiO_2 interface touching the photodiode. It is conceivable that a metastable bond rotation would change a trap state energy to be closer or further away from the center of the band gap, creating the conditions necessary to produce the observed signal. Or, perhaps a charge trap located on the boundary of the SCR would move the depletion edge depending if it was in the capture or emission state. Regardless, this noise source is differentiated from SF-RTS by the fact that the RTS amplitude is a function of integration time, and its very long time constants [5]. Since the form of RTS noise changes the dark current level in a pixel by a discrete amount, it has been denoted as Dark Current RTS (DC-RTS) [6].

3.2 SF-RTS Noise

SF-RTS noise theory is based on the Shockley-Read-Hall statistics that describe the emission and capture of electrons to/from the valance or conduction band [7]. As such, the time constant for a filled trap, or capture state reads as $\frac{1}{\tau_c} = \sigma_t \bar{v} n$ and for an empty trap or, emission state $\frac{1}{\tau_e} = \sigma_t \bar{v} N_c \exp\left(\frac{E_t}{kT}\right)$

where σ_t is the trap cross section, $\bar{v}$ the mean thermal velocity of the electrons, n is the electron density in the conduction band, N_c is the effective density of states, E_t is the trap energy, k is Boltzmann's constant, and T is the temperature [4]. Studying these trap states via RTS provides a unique tool set to characterize MOSFET device defects.

CHAPTER FOUR – DC-RTS NOISE

4.1 Experimental Investigation of DC-RTS Noise

As stated previously, DC-RTS is a noise source characterized by a discrete change in the dark current of a pixel, identified by integration time dependence on RTS amplitude and time constants which are characteristically much longer than SF-RTS. What remains elusive is the mechanism behind this noise source.

In order to study characteristics of DC-RTS amplitudes and time constants, five commercial-off-the-shelf (COTS) Omnivision OV5647 CMOS image sensors were irradiated at the Oregon Health Sciences University Radiation Department. These sensors have a full well capacity of $4.3k$ electrons as reported by Omnivision [12] and a 10-bit ADC giving an e^-/DN conversion of approximately 4.2 electrons per digital number. Linearity of the device was confirmed by Belloir et. al. [13], and our own group. The chips were dosed, unbiased, with a continuum of high energy gamma and x-rays created by a linear electron accelerator with a peak energy of $2\ MeV$. Ionizing radation is a well documented underlying cause of RTS behavior, that creates defects on the Si/SiO_2 interface, including the shallow trench isolation (STI) [14].

Frames for all imagers were taken in dark conditions with six second integration times at a temperature of $32℃$.

CHAPTER FIVE – HAAR WAVELET ANALYSIS

5.1 The Discrete Wavelet Transform

Central to the following RTS noise characterization is the discrete wavelet transform. While there are a variety of suitable wavelets that can be used to perform the transform, here, I will be utilizing the Haar wavelet as it has produced excellent results.

To understand how the discrete wavelet transform works with the Haar wavelet consider a one dimensional vector **f** made of N sampled elements, $(\mathrm{f}_1, \mathrm{f}_2, \mathrm{f}_3, \ldots \mathrm{f}_\mathrm{N})$ such that

$$\mathbf{f} = (\mathrm{f}_1, \mathrm{f}_2, \mathrm{f}_3, \ldots \mathrm{f}_\mathrm{N}) \qquad (1)$$

To perform the wavelet transform we take the raw signal **f** and use it to create two daughter vectors **a** and **d**, each of which are half the length of signal **f** [8]. The **a** series is the trend or average series, and its coefficients are derived from the original signal as a running average such that:

$$a_m = \frac{f_{2m-1}+f_{2m}}{2} \qquad 1 < m \leq N/2 \qquad (2)$$

The **d** series is called the details vector and its coefficients track the changes in the original signal similar in function to a derivative:

$$d_m = \frac{f_{2m-1}-f_{2m}}{2} \qquad 1 < m \leq N/2 \qquad (3)$$

Of course, since a transform is performed, it is necessary there be an inverse transform as well. For the Haar wavelet transform, the original signal can be recovered as follows:

$$\mathbf{f} = \left(\frac{a_1+d_1}{2}, \frac{a_1-d_1}{2}, \ldots \frac{a_{\frac{N}{2}}+d_{\frac{N}{2}}}{2}, \frac{a_{\frac{N}{2}}-d_{\frac{N}{2}}}{2}\right) \quad (4)$$

It should be noted here that all the coefficients in both the trend and details series are multiplied by $\sqrt{2}$ in order to ensure that the total energy of the signal (the sum of the squares of the samples) is conserved throughout the transform.

A key feature of the wavelet transform is multi-resolution analysis (MRA). It is MRA that allows the wavelet transform to act like a microscope for digital signals, picking out key features at any scale of interest [9]. For example, if one is interested in features that occur on longer time scales it may be beneficial to perform the Haar wavelet transform several times, first to the original signal, then to its trend daughter signal, and so on. Each transform produces a trend and details series half the size of the signal from which they were derived, and therefore each coefficient in subsequent levels represents 2^k values from the raw signal, where k is the number of levels.

Now, with all the pieces laid out, we can construct a series of Haar details operators **W** and Haar trend operators **V** which are scalar multiplied with the original signal to create the sets of coefficients. For the first level (highest resolution) analysis:

$$\mathbf{W}_1^1 = \left(\frac{1}{\sqrt{2}}\right)(1, -1, 0, 0, 0, 0, \ldots)$$

$$\mathbf{W}_2^1 = \left(\frac{1}{\sqrt{2}}\right)(0, 0, 1, -1, 0, 0, \ldots)$$

The first level details coefficients are then generated as follows:

$$d_1 = \frac{f_1 - f_2}{\sqrt{2}} = \mathbf{f} \cdot \mathbf{W}_1^1$$

$$d_m = \mathbf{f} \cdot \mathbf{W}_m^1$$

Note that the superscript on the operator represents the level of resolution. So, the details operator to find the m^{th} element of the k^{th} level transform is represented as $\mathbf{W}_m^k$.

The trend operators are likewise constructed:

$$\mathbf{V}_1^1 = \left(\frac{1}{\sqrt{2}}\right)(1, 1, 0, 0, 0, 0, \dots)$$

$$\mathbf{V}_2^1 = \left(\frac{1}{\sqrt{2}}\right)(0, 0, 1, 1, 0, 0, \dots)$$

Similar to the details coefficients:

$$a_1 = \frac{f_1 + f_2}{\sqrt{2}} = \mathbf{f} \cdot \mathbf{V}_1^1$$

$$a_m = \mathbf{f} \cdot \mathbf{V}_m^1$$

5.2 Wavelet Denoising

The key step in the RTS analysis algorithm is denoising the original signal using the coefficients generated by the discrete wavelet transform (DWT). This method is particularly useful for detecting and characterizing RTS pixels because it suppresses white noise while leaving larger sudden changes untouched. It is in a way, similar to a high-pass or low-pass filter that is dependent on change in magnitude rather than frequency.

Firstly, the DWT is performed and the details vector coefficients are examined. If a particular coefficient falls below a specified threshold, it is simply set to zero. If a

coefficient is larger than the threshold, it is either untouched (hard thresholding), or is subtracted by the threshold value (soft thresholding).

This threshold itself can be derived by a variety of techniques. The threshold chosen here is the VisuShrink, or Universal Threshold. This threshold, laid out by Donoho and Johnstone [10] is

$$\mathrm{T} = \hat{\sigma}\sqrt{2\log(n)} \tag{5}$$

where n is the number of elements in the discrete signal and $\hat{\sigma}$ is an estimate of the noise equal to the median of the absolute values in the details vector, $median\{\mathbf{d}\}$ divided by $u_{0.75} = 0.6745$, the 0.75 quantile of a normal distribution [11].

Though there are a variety of thresholds to choose from, the Universal Threshold is an ideal choice since it usually underfits the data, or in this case, minimizes the number of false RTS events.

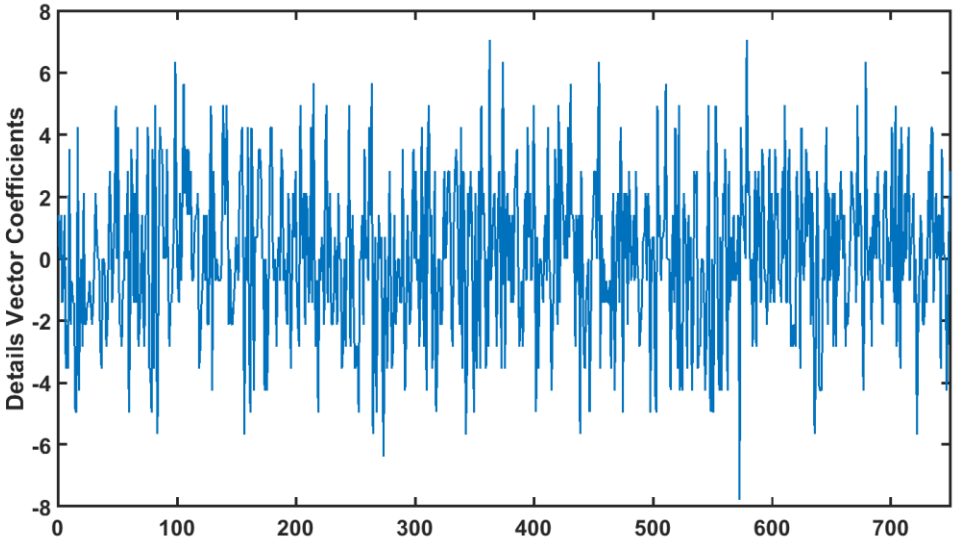

Figure 8: A typical details vector before thresholding

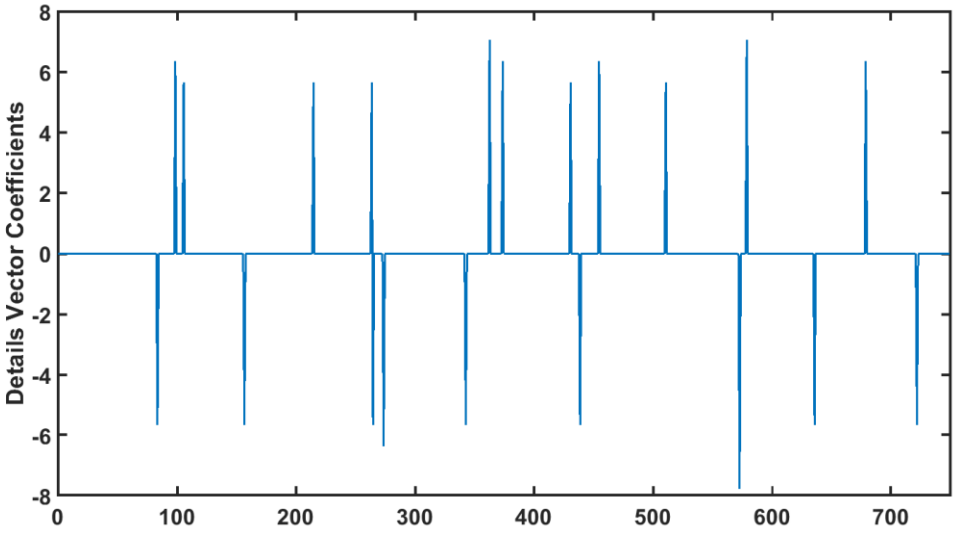

Figure 9: A typical details vector after thresholding

Recall that the details vector of the wavelet transform is generated by the changes in the original signal. As seen in figures 8 and 9, thresholding a details vector can greatly simplify, or reduce the noise power in the original signal, making the task of analyzing only the RTS noise far more manageable.

CHAPTER SIX – APPROXIMATE SIGNAL CONSTRUCTION

In order to analyze RTS amplitude and time constant distributions in radiation damaged sensors a noise free (RTS exempt) approximation signal is constructed based on the raw output from a particular pixel over several hours. The following process is designed to be highly discriminatory when validating a pixel for exhibiting RTS behavior. This is done to prevent false positive RTS detection from characteristics like high white noise, pink noise, or single events like cosmic ray impacts from polluting the statistics pool.

6.1 Window Comparison

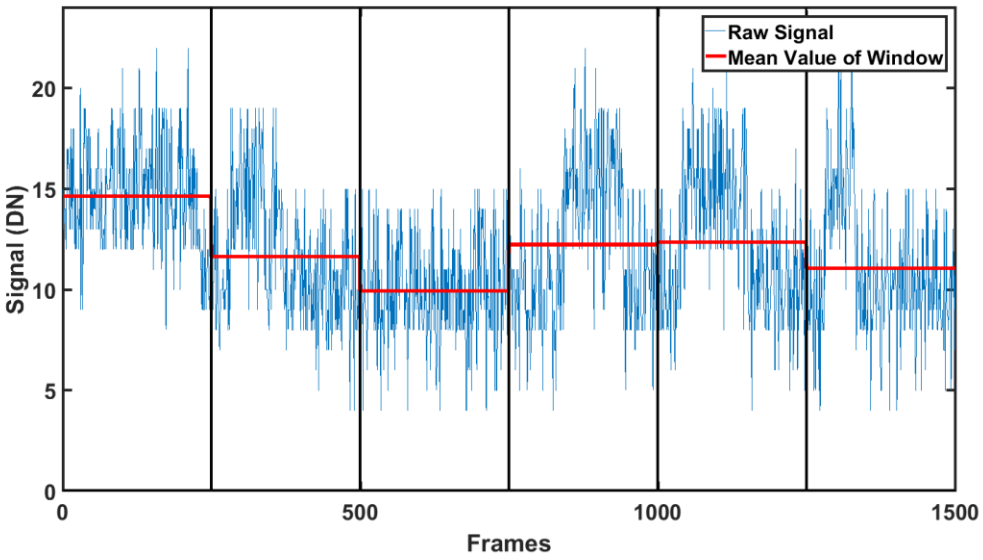

Figure 10: Stage 1, the raw signal **f** is split into windows of size 250 frames. The mean values of a window is compared to the mean of the previous two windows

The first step in the construction process is simply to break up the raw pixel signal into sections and compare the mean values of adjoined sections and their neighbor. This crude but effective RTS-Noise detector uses the standard deviation, σ_r of a signal as the metric for RTS candidacy. If the mean value of a particular section is greater or less than the mean value of the previous section by at least σ_r the pixel is passed along for analysis. We have chosen here to use six windows representing 250 frames. This first simple step is important to the process not only because it does very well picking out RTS pixel candidates, but also because it saves precious run time by ensuring the computational heavy lifting is only performed on signals of interest. If a pixel fails the window comparison, the program simply moves on to the next.

6.2 DWT Denoising

A pixel that passes the window comparison test is then run through the DWT denoising process described above. The following analysis utilized a 7-level denoising analysis.

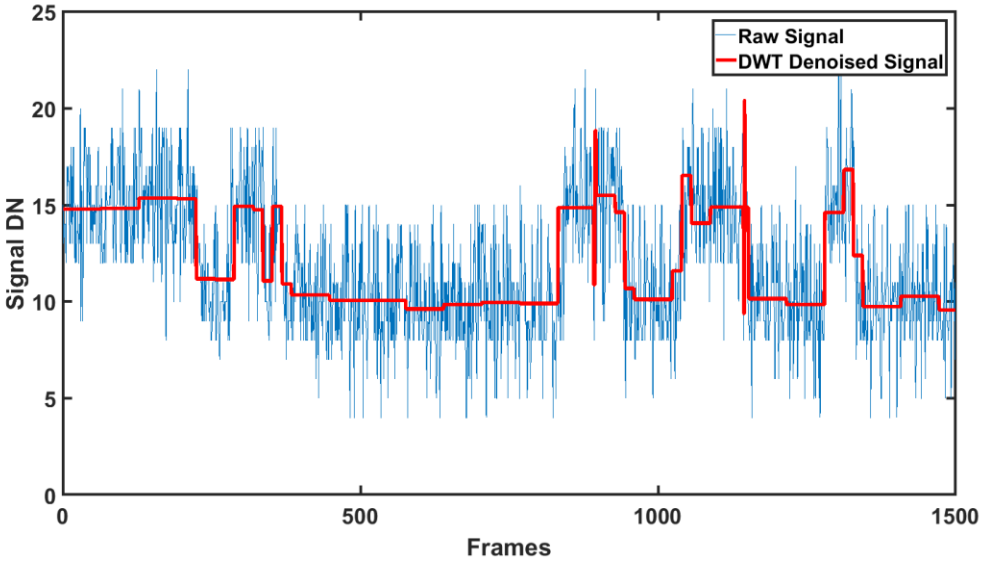

Figure 11: Stage 2, the signal f is run through the DWT denoising process, detailed above, and returned as the denoised signal $\mathbf{f}'$. Though the white noise is severly depressed, transient spikes remain

6.3 Temporal Screen

The denoising process cleans the signal, however issues remain. First, the magnitude of the RTS transition amplitudes in the approximation often fall short of their true value, leaving a systematic error in our reporting. Second, very brief transitions appear in this denoised version, but are too short to make any analytical sense. Since these features often fall outside of the Nyquist limit, they must be disregarded as transients in the characterization. In order to screen these brief transitions from the approximation signal temporal thresholding phase is employed in the program. This is accomplished by simple comparison and is possible because of the nature of the DWT denoising process. As seen in Figure 11, DWT denoising can leave long runs of

sequential frames with exactly the same value. This means that in order to verify that a particular transition is not transient, all that is needed is to compare frame k with frame $k-1$. If there is some difference in their values it is understood that a transition has taken place. Then, we compare the value of frame k with the value of the next l frames where l is the width of our temporal screen. If in fact the value of k is the same as the next l frames, the value is kept. If it fails this condition the value of frame n is set to the value of frame $k-1$. The width of this screen can vary and is admittedly subject to debate. On the one hand, the goal should be to construct a signal that is as closely correlated to the original as possible. On the other, many RTS signals display amplitudes that barely exceed the white noise, which can cast doubt on their very existence. In order to further increase the confidence of a transition we have chosen to set l equal to 10.

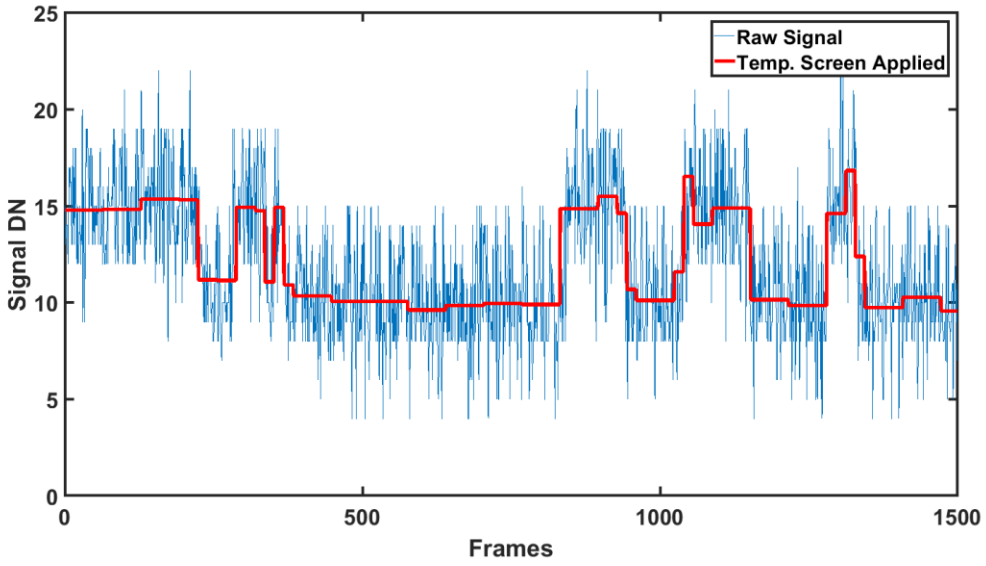

Figure 12: Stage 3, the denoised signal $\mathbf{f}'$ is passed through the temporal screen and returned as the denoised and screened signal $\mathbf{f}''$ Transient spikes have been removed

6.4 A Second Thresholding

At this point the signal shows almost no remnant of the white noise. With the transients removed and the majority of the heavy lifting taken care of by the DWT denoising, all that remains is to again threshold the changes in the screened signal. Recognizing that most of the changes, sample to sample, are zero, and only the largest changes are RTS transitions, the goal is to remove the smaller variations left over from the DWT denoising process. This time, rather than the dyadic DWT, we simply create a new series of size $N-1$ by subtracting each value from the preceding one starting with element two. Here N is, again the number of elements in the signal and $\mathbf{f}'$ is the members of the screened signal. **s** is used in place of **d** to emphasize the non-dyadic quality of this last details vector.

$$\mathbf{s} = (\mathrm{s}_1, \mathrm{s}_2, \mathrm{s}_3, \ldots \mathrm{f}_{\mathrm{N}-1}) \tag{6}$$

$$s_m = f'_m - f'_{m-1} \tag{7}$$

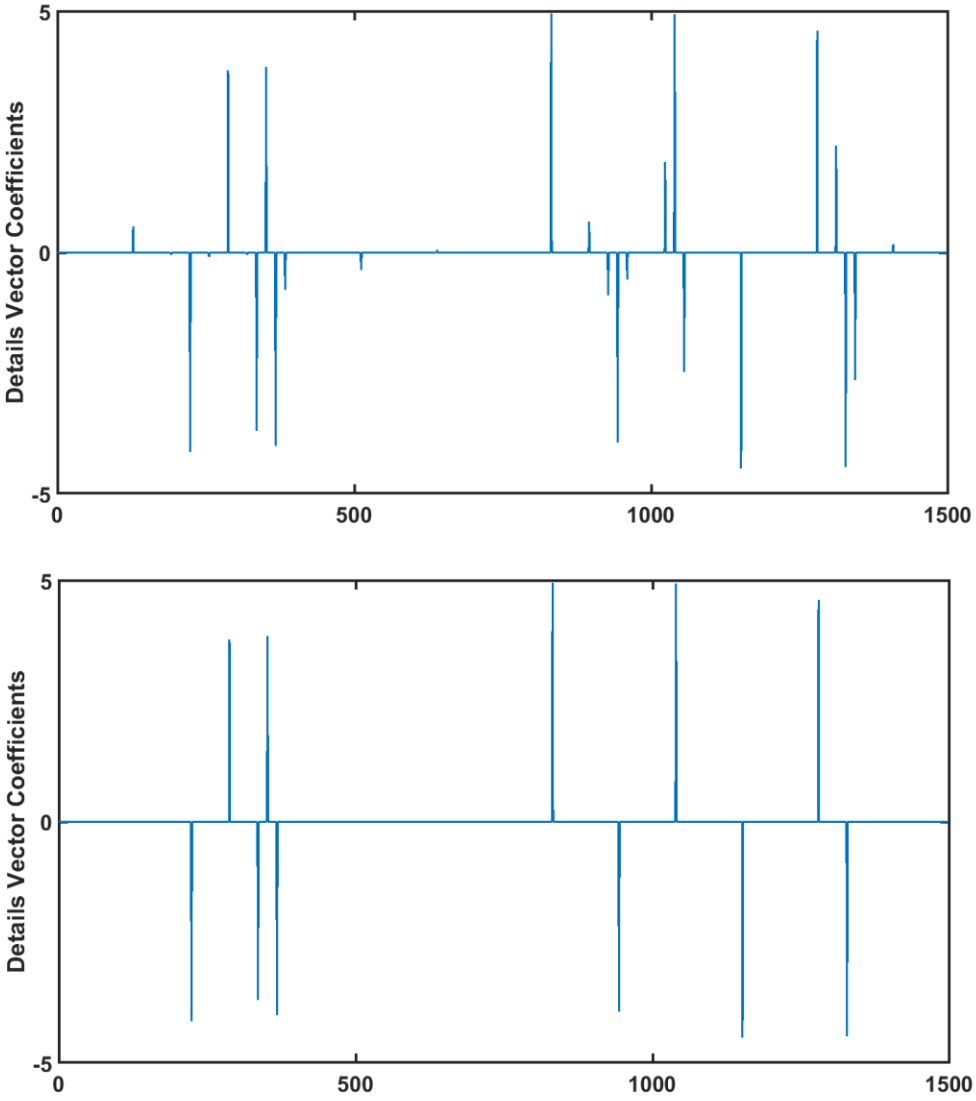

Figure 13: Stage 4, a typical details vector before and after denoising. All but a few of the elements are set to zero

Again, the threshold is applied to this series just as before, but now the threshold is chosen differently. Since there are now so few large changes representing RTS transitions, and some smaller ones left over from the DWT process, we set the threshold

$T_s = s_{MAX} * u_{0.75}$ [11]. All elements smaller than the threshold are again set to zero, while those larger are untouched.

6.5 Final Reconstruction

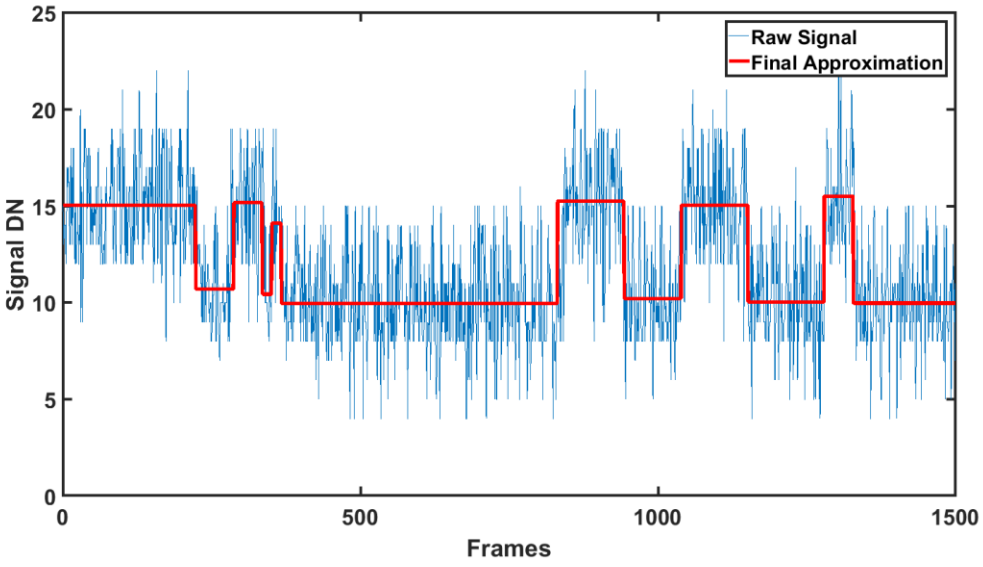

Figure 14: Stage 5, The final approximation is constructed. From here RTS transition amplitudes and time constants can be collected for statistical analysis

For the final approximate form the locations of the remaining non-zero elements are taken from the second threshold series, **s** and the mean values of the original signal between those locations are used to fill in the approximation. By using the mean value of the raw signal between transitions, it is ensured that the final amplitudes are very close to the actual values. From this form it is simple to collect time constants and transition amplitudes from tens of thousands of RTS pixels and study them from a statistical perspective.

7.1 RTS Analysis

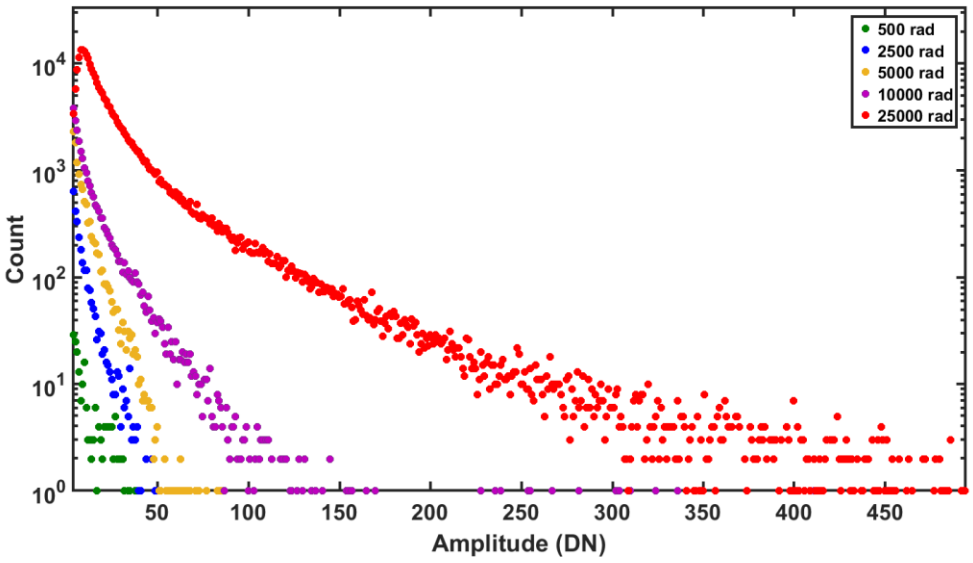

Figure 15: The distribution of RTS transition maximum amplitudes

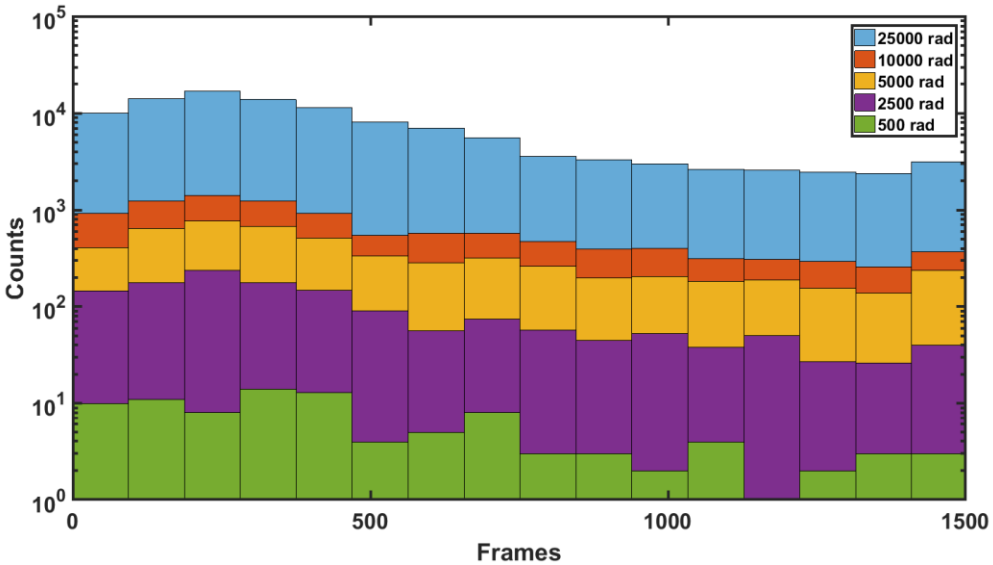

Figure 16: The distribution of 'high' state time constants

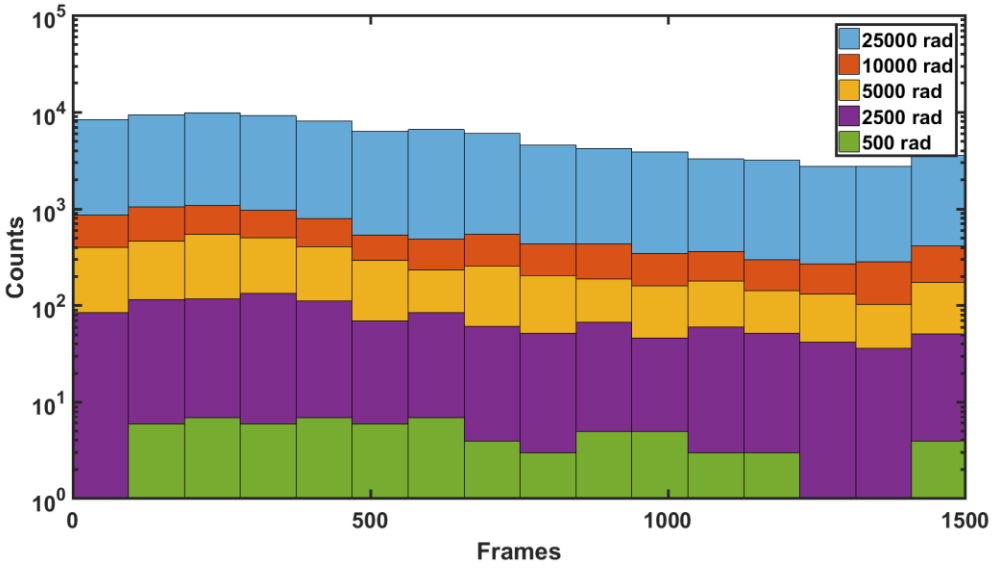

Figure 17: The distribution of 'low' state time constants

The semilogrithmic plot of the distribution of maximum RTS transition amplitudes in Figure 15 reveals that, as expected, larger dose leads to more RTS pixels. The amplitudes observed in this analysis can reach very large magnitudes, up to $350e^{-}/s$, though magnitudes of over $10000e^{-}/s$ have been reported [14]. It is notable that the slopes of the curves share a similar shape in all of the semi-log histogram curves, indicating that a higher dose increases the probability of creating a metastability, but the amplitude probability is set.

Similar to the maximum amplitude plot, the time constant histograms of Figures 16 & 17 display an exponential distribution, here with a peak approximately 250 frames, or around 85 minutes. It is likely that the shortest transition times are artificially suppressed by choosing to denoise the signals down several levels. A signal that is denoised four levels would yield a high-resolution analysis at the cost of approximation accuracy from false positives. A curiosity from the plots is the apparent flattening of the

distribution peak seen in the 'low state' time constants, i.e., the lower of the two level dark current signal levels. This may indicate that the physical configurations that produce the 'low state' for DC-RTS pixels are, on average, more stable than the 'high state' configuration.

7.2 Second-Order Defect Generation

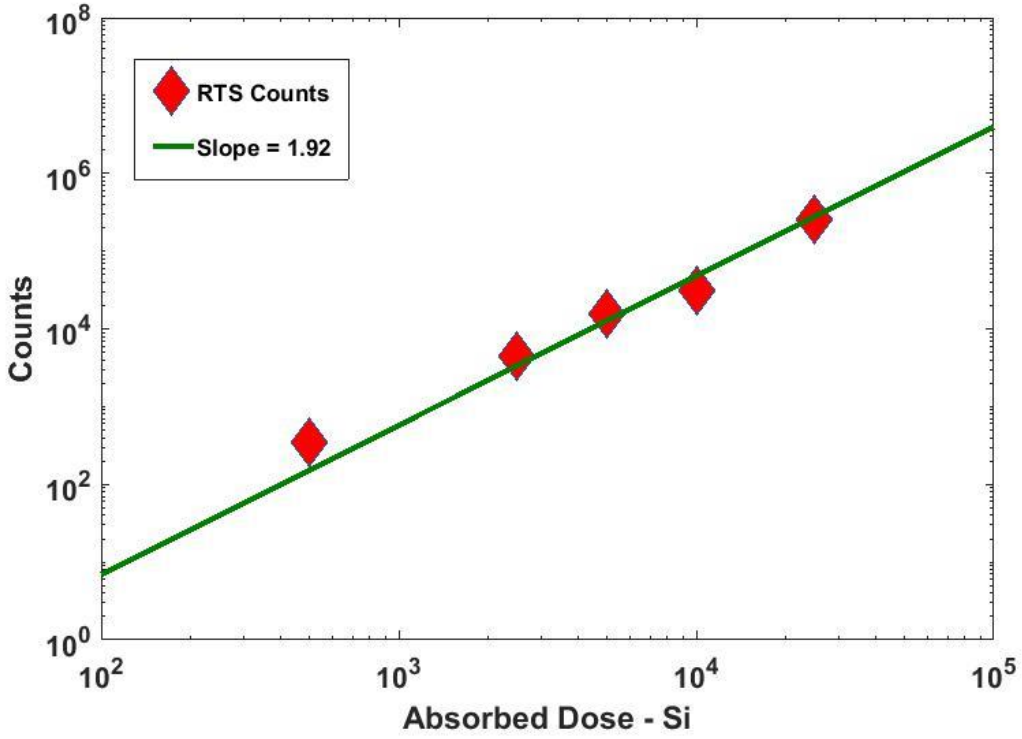

Figure 18: The number of RTS defect centers as a function of absorbed radiation dose

The number of RTS pixels does not follow a linear correlation with radiation dose, but rather $counts \propto dose^{\sim 2}$. This result indicates that the process creating RTS centers by γ-radiation is of second-order. There is some precedent for this type of defect

generation mechanism. It has been reported that very high doses of γ-radiation is responsible for the formation of defect centers known as $H\ (97K)$ and $I^{0/-}\ (200\ K)$, designated as such by their peaks on a TSC spectrum. The I center band energy has been measured at $0.5eV \pm 0.05eV$ below the conduction band. There is some discussion as to whether or not H is simply the donor state of I, making them the same defect. Regardless, both states grow in population at a nearly quadratic rate with dose and share the same slope on a log-log plot, as the data reported in Figure 18 [15]. This defect is suggested to be the double vacancy oxygen (V_2O) complex which can be formed when a γ-ray strikes a vacancy oxygen defect, i.e., $V + O \rightarrow VO$, then $VO + V \rightarrow V_2O$.

While far from conclusive, the abundance of oxygen on the STI inclusion interface, combined with the measured band energy of I, which is close to the mid-gap and therefore well suited for SRH G/R, as well as the second-order generation of the defects all seem to suggest that the V_2O complex is a reasonable candidate for RTS centers. It has additionally been reported that defects in more complex devices (In-Ga-Zn-O transistors) display metastability between a vacancy and local oxygen, strengthening this claim [16].

CHAPTER EIGHT – CONCLUSIONS AND DISCUSSION

RTS noise is a ubiquitous physical phenomenon with unique sources everywhere. There are at least two different kinds of RTS in CMOS image sensors alone, and perhaps three, if DC-RTS in the bulk of the diode has a different mechanism than DC-RTS in the oxide. Since nearly all physical processes are measured with a current or a voltage, it is not uncommon to observe the characteristic RTS signal in a variety of physical fields, where some small discrete physical change leads to a significant impact on the final measurement. This is the case with calcium ion transport in lipid membranes, which open and close like an annulus [17].

A new technique was developed in order to analyze the RTS noise and extract its key parameters. This approach utilizes wavelet denoising and simple arithmetic to remove thermal noise from a time based signal, while preserving RTS transitions for analysis. Wavelet denoising is similar in purpose to a high pass filter, but is designed to mute noise power derived from small changes in signal level rather than low frequency sources. This makes it, by design, naturally suited for RTS analysis since RTS is defined by discrete shifts in signal level. By adding a time based screen, it is ensured that any large shift in signal that ends up in the statistical pool is indeed RTS and not from a single event, e.g., cosmic rays.

The results obtained from this methodology produce similar results to those seen in investigations into radiation effects on CMOS image sensors [14], [5]. Where this study goes beyond that previous work is in the possible identification of the type of

defect that produces this effect. The V_2O complex is a convincing candidate for this particular RTS center, but needs to be studied further.

The analysis tools developed here will be utilized in the characterization of RTS pixels in a CCD imager. Since RTS noise in image sensors arises from either the capture and emission of a charged particle, or the metastability of a generation/recombination (G/R) center, it provides a unique ability to study lattice defects on a highly localized level. By using a CCD, which lacks an in-pixel amplifier, the known source location of SF-RTS noise, it is expected to exclusively observe RTS noise that arises from metastable G/R, which is still not well understood.

REFERENCES CITED

[1] R. Fontaine, “The Evolution of Pixel Structures for Consumer-Grade Image Sensors,” in IEEE Transactions on Semiconductor Manufacturing, Vol. 26 No. 1, pp.11-16, February 2013.

[2] T.J.Cunningham, B.Hancock, C. Sun, G. Yang, M. Ortiz, C. Wrigley, S. Seshadri, and B. Pain. “A Two-Dimensional Array Imager Demonstrating Active Reset Suppression of kTC-Noise,” In IEEE Workshop on Charge-Coupled Devices & Advanced Image Sensors, Elmau, Germany, May 2003.

[3] V., “Radiation Effects on CMOS Active Pixel Image Sensors,” in Ionizing Radiation Effects in Electronics: From Memories to Imagers (M. Bagatin and S. Gerardin, eds.), CRC Press, 2015.

[4] E. Hoekstra, “Large Signal Excitation Measurement Techniques for RTS Noise in MOSFETs,” in EUROCON 2005 - The International Conference on ”Computer as a Tool”, vol. 2, pp. 1863–1866, Nov. 2005.

[5] V. Goiffon, P. Magnan, P. Martin-Gonthier, C. Virmontois, and M. Gaillardin, “New source of random telegraph signal in CMOS image sensors,” 2012.

[6] V. Goiffon, G. R. Hopkinson, P. Magnan, F. Bernard, G. Rolland, and O. Saint-Pe, “Multilevel RTS in Proton Irradiated CMOS Image Sensors Manufactured in a Deep Submicron Technology,” IEEE Transactions on Nuclear Science, vol. 56, pp. 2132–2141, Aug. 2009.

[7] T. B. Tang, A. F. Murray, and S. Roy, “Methodology of Statistical RTS Noise Analysis With Charge-Carrier Trapping Models,” IEEE Transactions on Circuits and Systems I: Regular Papers, vol. 57, pp. 1062–1070, May 2010.

[8] J. S. Walker, A Primer on Wavelets and their Scientific Applications. Boca Raton [Fla.]: Chapman & Hall/CRC, 2nd ed., 2008.

[9] M. Gilli, Computational Economic Systems: Models, Methods & Econometrics. Springer Science & Business Media, Mar. 2013.

[10] G. P. Nason, “Choice of the threshold parameter in wavelet function estimation,” Wavelets and statistics, vol. 103, pp. 261–280, 1995.

[11] J. Groß, Linear Regression. Springer Science & Business Media, July 2003.

[12] Omnivision, “Ov5647 5-megapixel product brief,” Nov. 2010.

[13] J. M. Belloir, V. Goiffon, C. Virmontois, P. Paillet, M. Raine, P. Magnan, and O. Gilard, “Dark Current Spectroscopy on Alpha Irradiated Pinned Photodiode CMOS Image Sensors,” IEEE Transactions on Nuclear Science, vol. 63, pp. 2183– 2192, Aug. 2016.

[14] E. Martin, T. Nuns, C. Virmontois, J.-P. David, and O. Gilard, “Proton and g -Rays Irradiation-Induced Dark Current Random Telegraph Signal in a 0.18-mm CMOS Image Sensor,” IEEE Transactions on Nuclear Science, vol. 60, pp. 2503–2510, Aug. 2013.

[15] Pintilie, I., Fretwurst, E., Lindström, G., Stahl, J. “Second-order generation of point defects in gamma-irradiated float-zone silicon, an explanation for ‘type inversion’,” Applied Physics Letters, vol. 82, pp. 2169-2171, Mar. 2013.

[16] Lee, S., Nathan, A., Jeon, S., and Robertson, J. “Oxygen Defect-Induced Metastability in Oxide Semiconductors Probed by Gate Pulse Spectroscopy,” Scientific Reports, vol. 5, pp. 1-10, Oct. 2015.

[17] Favero, Terence G. and Webb, Jason and Papiez, Maria and Fisher, Erin and Trippichio, Robert J. and Broide, Michael and Abramson, Jonathan J. “Hypochlorous acid modifies calcium release channel function from skeletal muscle sarcoplasmic reticulum,” Journal of Applied Physiology, vol. 94, pp. 1387-1394, Apr. 2003.